

Characterization of dSiPM-based TOF-PET detector modules for proton therapy verification

*Bachelor research thesis Physics of Life and Health
University of Groningen, KVI-CART*

Martijn Middelkamp - s2407957



rijksuniversiteit
 groningen

kvi - center for advanced
 radiation technology

Supervisor:

- Dr. P.G. Dendooven

Daily supervisor:

- Dr. K. Brzezinski

Abstract

This bachelor thesis project presents a study of the characteristics of time-of-flight positron emission tomography (TOF-PET) detector modules based on digital silicon photomultiplier array (dSiPM) which are made by Philips Digital Photon Counting. Multiple experiments were performed using a ^{22}Na radioactive source to get more insight into the characteristics of these detectors, especially regarding to TOF-PET imaging of proton beam therapy for cancer treatment. The efficiency of the setup for coincidence measurements was investigated as a function of the position of the source in the mid-plane perpendicular to both opposing detector modules. It is found that this efficiency map was cone-shaped with its maximum of 0.25 % exactly in the centre. Time skews of the detector module elements were determined and coincidence measurements were corrected for these skews. It turned out that this correction improved the time resolution of coincidence measurements by 36 % when the source is placed exactly at the midpoint between the detectors. The performance of the setup was investigated for different photon count rates by varying the distance between the source and the detector. It was found that a pile-up or saturation of detected photons occurs when the ^{22}Na source is placed very close towards the detector. Also, a smaller distance between the source and detector has a negative effect on the time resolution. Finally, the intrinsic radioactivity of the LYSO scintillation crystal of the detectors was investigated. This intrinsic radioactivity was clearly visible in the energy spectra, but by selecting a proper time window for the 511-keV photon peak, it could be substantially filtered out.

Contents

1	<hr/>	
	Summary	3
2	<hr/>	
	The basics of proton therapy and PET imaging	5
2.1	Proton therapy	5
2.1.1	Ionizing radiation - Interaction of particles with matter	7
2.1.2	Formation of radionuclides	9
2.2	PET imaging	9
2.2.1	Ionizing radiation - Interaction of electromagnetic radiation with matter.	11
2.2.2	PET detectors	12
3	<hr/>	
	Experimental Setup	16
3.1	Materials	16
3.1.1	Philips Digital Photon Counting detectors	16
3.1.2	Detector operation	18
3.2	Experimental methods	20
3.2.1	Detector efficiency	20
3.2.2	Time skew correction	21
3.2.3	High count rate performance	22
3.2.4	Intrinsic radioactivity	25
4	<hr/>	
	Results	27
4.1	Detector efficiency	27
4.2	Time skew correction	28
4.3	High count rate performance	29
4.3.1	Effect on timing and energy resolution	30
4.4	Intrinsic radioactivity	32

Discussion and Conclusion	34
5.1 Detector efficiency	34
5.2 Time skew correction	34
5.3 High count rate performance	35
5.3.1 Effect on time and energy resolution	36
5.4 Intrinsic radioactivity	37
Appendix A PDPC instructions	41
Appendix B Time Skew Correction	44

Chapter 1

Summary

Proton therapy is a rapidly expanding cancer treatment that uses a proton beam to irradiate diseased tissue instead of photons, as in conventional radiation therapy. It was Robert Wilson, regarded as the father of proton therapy, who in the 1940s already suggested the potential usage of protons in cancer treatment therapy due to their advantageous dose distributions [1]. The main reason to choose proton therapy over conventional photon therapy is that the radiation dose, the energy imparted to matter per unit mass, of the proton beam is deposited over a narrow range, resulting in very little dose in front of the tumor and almost no dose behind. Protons, as do all charged particles, have a very rapid energy loss in the last few millimeters of penetration. This results in a sharply localized peak of dose, known as the Bragg peak.

To make sure the dose is deposited at the proper desired location, positron emission tomography, PET, can be used to trace back the deposited proton beam dose. The rationale for using PET is that as the protons enter the patient and interact with the elements in tissue, there are inelastic collisions that produce positron emitters [3]. The two 511-keV annihilation photons produced by the positron-electron annihilation are detected by two opposing detectors consisting of a scintillation crystal and a photo sensor. The most used photo sensors are vacuum photomultiplier tubes (PMT). However, an alternative device, the Silicon photomultiplier (SiPM), has various advantages compared to PMT's. These advantages are ruggedness, compactness, insensitivity to magnetic fields, low operating voltage, low power consumption and large scale fabrication [4].

This bachelor research project for Physics is about the characteristics of time-of-flight positron emission tomography (TOF-PET) detectors based on dSiPM's, which are provided by Philips Digital Photon Counting, in the framework of proton therapy verification. The positron emitter used in the experiments was by a radioactive ^{22}Na source. The efficiency of the detectors was measured as a function of the source position, the timing resolution was investigated, as well as the energy resolution. Detection at high count rate was explored and the intrinsic radioactivity of the scintillation LYSO-

crystal has been tested. An in-depth knowledge of the operation of the detector modules was required along with the ability to process and analyse the raw data files.

The outline of this report is as follows. First some theoretical concepts about ionizing radiation are discussed concerning the interaction of radiation with matter. Next, the working principle of PET, as well as its usage in proton therapy verification, and a description of Geiger-mode single photon avalanche diode (SPAD) cells for photon detecting is discussed. Then the materials and methods are discussed, and the detector modules used in this project are described, as well as the experiments that will be done with them. Finally, the results of these experiments are discussed followed by a discussion and conclusion.

Chapter 2

The basics of proton therapy and PET imaging

Proton therapy verification with PET deals with a variety of subjects related to physics, so for that purpose it is interesting to dig deeper into these subjects and gain more knowledge of them. As mentioned before, in the whole process of proton therapy verification with PET, a patient first gets irradiated with a proton beam, creating positron emitters in the patients tissue which then generates annihilation photons that can be detected by the appropriate detectors to image the dose deposition.

For reasons of clarity, the subjects in this chapter are placed in chronological order, that means in order from irradiating/treatment to imaging. The relevant background information on the physical processes happening during proton therapy are discussed first, followed by the physics of monitoring the dose deposition of the proton beam treatment. This chapter is roughly divided into "treatment" and "imaging". In the treatment section we basically discuss the interaction of (charged) particles, especially protons, with matter and the link to detection is made by explaining the formation of radioactive isotopes in the irradiated tissue. Then the text focuses on how these radioactive isotopes, or radionuclides, are useful for imaging by PET. The theoretical concepts of the interaction of photons with matter are explained, followed by the working principle of PET and at last, we dig deeper into the photon detection mechanisms.

2.1 Proton therapy

Radiotherapy is an essential component of cancer or tumor therapy. Proton therapy is a type of external beam radiotherapy that uses ionizing radiation. Because of ionization, the radiation damages molecules within the cells, especially the DNA or genetic material. Damaging the DNA destroys specific cell functions, particularly the ability to divide or proliferate and thus destroying the tumor which will be irradiated.

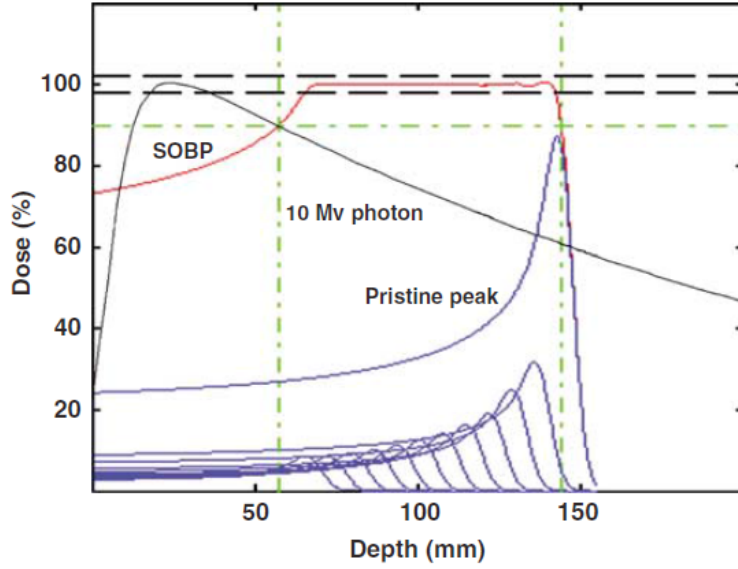


Figure 2.1: Dose vs depth curves for a spread out Bragg peak (in red), its pristine proton beam Bragg peaks (in blue), and a photon beam created by 10 MeV electrons (in black) for comparison [2].

Protons, as do all charged particles, have a very rapid energy loss in the last few millimeters of penetration. This results in a sharply localized peak of dose, known as the Bragg peak, which is illustrated in figure 2.1. Unlike a photon beam, which has a high entrance dose and decreases in intensity gradually while passing through the body, a proton beam can penetrate through tissues and deposit most of its energy near the end of its track. Proton therapy is thus one of the most precise and accurate external radiation therapy modalities. The depth of the Bragg peak depends on the energy of the proton beam and on the type of tissue it traverses. By using protons of multiple energies it is possible to create a so called spread-out Bragg peak (SOBP) field [2].

Due to the proton Bragg peak, proton therapy has a big advantage compared to conventional photon therapy when it comes to dose delivery. First proton therapy has a much lower entrance dose and no dose beyond the target volume. Also, it has lower integral dose, thus the probability of secondary tumor caused by radiation dose to the normal tissue is lower [11]. Therefore, the same radiation dose to the tumor can be achieved with lower integral dose to the normal tissue, or the dose to the diseased tissue can be increased by keeping the integral dose to normal tissue the same.

However, there are still some difficulties regarding proton therapy. Beside the fact that proton therapy has relative high capital cost, it is also more sensitive to uncertainties in treatment planning and delivery compared to photon therapy. There is under-shooting and over-shooting. Under shooting refers to the consequence of a range error where a portion of the tumor is not receiving any radiation dose because that part of the tumor lies after the last (highest energy) proton Bragg peak. On the other hand, when the bragg peak falls after the tumor, we are speaking of over-shooting. Here the

normal tissue is getting full unnecessary dose. This is especially of concern when the tumor is near a critical tissue structure [11].

In proton therapy, the dose delivery profile of one proton beam consists of two components. The longitudinal dose profile results mainly from the inelastic electromagnetic interaction with atomic electrons, which slows down the incoming protons. The lateral dose profile is dominated by the elastic scattering on the target nuclei, leading to a change in direction of the proton and thus a broadening of the beam.

2.1.1 Ionizing radiation - Interaction of particles with matter

Let's have a look at the physics of proton therapy. The term ionizing radiation refers to radiation that carries enough energy to free electrons from atoms or molecules and ionize them. In nuclear medicine ionizing radiation is useful mainly in two ways: for cancer treatment and medical imaging. To explain the interaction of radiation with matter, a distinction is made between radiation in the form of (charged) particles, that carry energy in the form of kinetic energy of mass in motion with momentum, and radiation in the form of electromagnetic waves, or photons, in which energy is carried by oscillating electrical and magnetic fields traveling through space at the speed of light. Both are of interest in proton therapy verification with PET since proton therapy deals with charged particles and PET deals with photons.

High-energy charged particles, such as protons or heavy ions, traversing matter lose energy primarily through the ionization and excitation of atoms. Due to the electromagnetic forces that the charged particles exert on the atoms, electrons will be knocked out of their orbit and leave the atom excited, in case the electron moves to an higher orbital, or ionized, in case the electron leaves the atom.

Figure 2.2 illustrates several mechanisms by which a proton interacts with an atom or nucleus: Coulombic interactions with atomic electrons, Coulombic interactions with the atomic nucleus, and nuclear reactions. To a first-order approximation, protons continuously lose kinetic energy via frequent inelastic coulombic interactions with atomic electrons. Most protons travel in a nearly straight line because the proton mass is 1832 times greater than that of the electron. In contrast, a proton passing close to the atomic nucleus experiences a repulsive elastic Coulombic interaction which, owing to the large mass of the nucleus, deflects the proton from its original straight-line trajectory. Inelastic nuclear reactions between protons and the atomic nucleus are less frequent but, in terms of the fate of an individual proton, have a much more profound effect. In a nuclear reaction, the projectile proton enters the nucleus; the nucleus may emit a proton, deuteron, triton, or heavier ion or one or more neutrons. Finally, proton Bremsstrahlung is theoretically possible, but at therapeutic proton beam energies this effect is negligible [5].

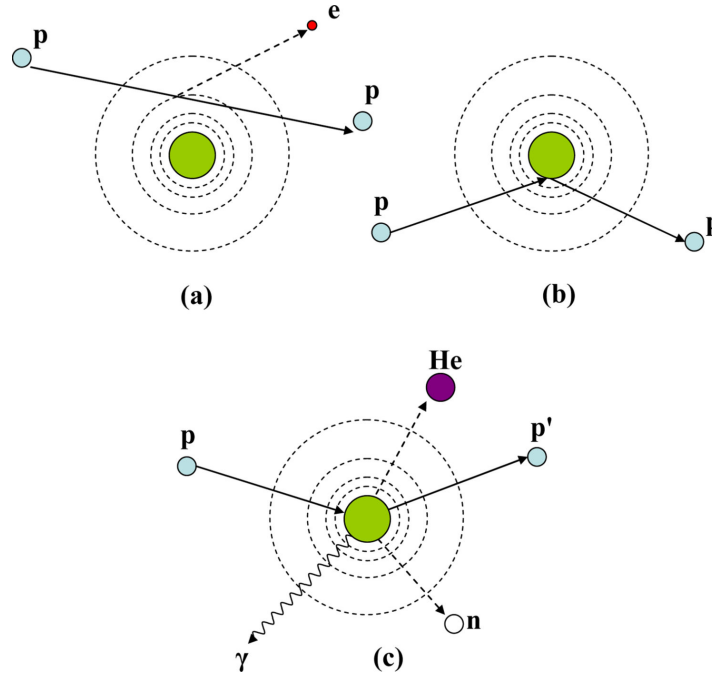


Figure 2.2: Interaction mechanisms of protons with an atom. (a) Coulombic interactions with atomic electrons. (b) Coulombic interactions with the atomic nucleus. (c) Nuclear reactions. [5].

Energy Transfer and Stopping Power

In radiation physics and dosimetry, the stopping power is an important quantity. The retarding force acting on charged particles by interaction with matter it travels through is defined as the stopping power, S , and basically describes the loss of particle energy. The stopping power is the sum of two processes: electronic stopping and nuclear stopping. Depending on the energy of the charged particles, one of the two will dominate. Electronic stopping describes the slowing down due to the inelastic collisions between bound electrons in the medium and the charged particle moving through it. The term nuclear stopping describes the elastic collisions between the charged particle and the nuclei of the atoms in the matter. Stopping power only describes the energy loss of charged particles, but not for uncharged particles, because of different interaction principles. The stopping power depends on the type and energy of the radiation and on the properties of the material it traverses. The stopping power of the material is mathematically described by the loss of energy per unit path length, and is usually expressed in $\text{keV}/\mu\text{m}$:

$$S(E) = -\frac{dE}{dx} \quad (2.1)$$

The linear energy transfer, LET, of a heavy charged particle in a medium is another quantity of fundamental importance in radiation physics and dosimetry and is

very much related to the stopping power [6]. The stopping power and LET concepts are different in the respect that total stopping power has the nuclear stopping power component, and this component does not cause electronic excitations. Hence nuclear stopping power is not contained in LET. A heavy charged particle traversing matter sometimes produces a secondary electron with sufficient energy to leave the immediate vicinity of the primary particle's path and produce a noticeable track of its own. Such a secondary electron is often called a delta, δ , ray. The difference between stopping power and LET is the fact that stopping power describes the rate of energy loss including the production of these δ rays, whereas LET neglects them.

Using relativistic quantum mechanics, a rigorous description of the energy loss rate is derived called the Bethe-Bloch formula. The mean energy loss per distance traveled for a particle with speed v , charge z (in terms of electron charge) and energy E can be described by the relativistic Bethe-Bloch formula [7]:

$$-\frac{dE}{dx} = \frac{4\pi}{m_e c^2} \cdot \frac{n z^2}{\beta^2} \cdot \left(\frac{e^2}{4\pi\epsilon_0}\right)^2 \cdot \left[\ln\left(\frac{2m_e c^2 \beta^2}{I \cdot (1 - \beta^2)}\right) - \beta^2\right], \quad (2.2)$$

where m_e is the electron mass and e is its charge, c is the speed of light in vacuum and n the electron number density. β is defined as v/c , ϵ_0 is the permittivity of the vacuum and I is the mean excitation potential of the medium.

2.1.2 Formation of radionuclides

During the irradiation of the protons to the diseased tissue, positron emitters are produced along the beam path through nuclear reactions. This will lead to a footprint of radio-tracers that are able to be detected with a PET scanner. For soft tissue, the most important species of radionuclide isotopes produced during irradiation are ^{11}C , ^{13}N and ^{15}O because of the abundance of carbon, nitrogen and oxygen in human tissue. Out of these three elements, ^{15}O has the most dominant contribution to the detectable radiation for dose deposition measurements during irradiation because of its relative short half-life of 2.037 minutes. For imaging several minutes after treatment, ^{11}C becomes more dominant with its half-life of 20.385 min [11].

2.2 PET imaging

Now that the relevant information of proton therapy is given, we should look at how the delivered dose of the proton beam can be recorded using PET. The signal in PET is produced by the annihilation of an emitted positron with an electron in the surrounding medium or tissue. This positron is generated by a β^+ decay process by radionuclides created by the proton beam interacting with the tissue. The annihilation mechanism is shown in figure 2.3. A positron is the antiparticle of an electron. When the positron combines with an electron in a so called annihilation reaction, their masses are converted

into energy in the form of photons. Positron annihilation leads to the production of two 511 keV photons emitted almost back-to-back, due to the conservation of energy and momentum. These photons are detected in time coincidence by the surrounding PET detectors to form a line-of-response (LOR).

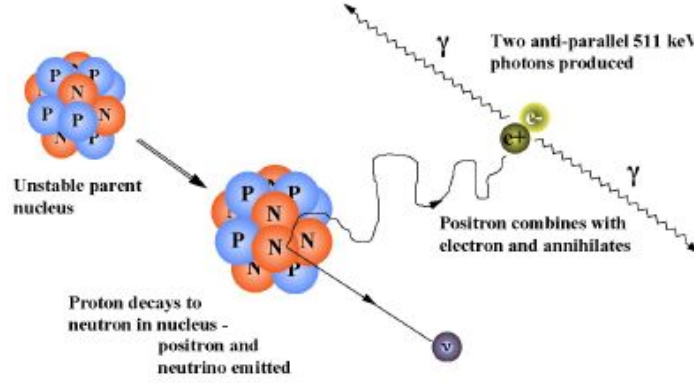


Figure 2.3: The emission of a positron via nuclear decay and the creation of 511 keV annihilation photons due to the positron-electron interaction [12].

The basic principles of time-of-flight positron emission tomography (TOF-PET) are shown in figure 2.4. In TOF-PET, the difference in the arrival times, dt of the two photons is measured with high precision. This helps localize the origin of the annihilation event along the LOR within a small region of the object. The uncertainty in this localization is determined by the system coincidence timing resolution, which is measured as the full-width-half-maximum (FWHM) of the histogram of TOF measurements from a point source. Although electronic circuits are capable of measuring timing differences of 0.001 nanoseconds, the rise times of light output from the scintillators currently available for PET imaging are too slow to provide this level of timing resolution. As well, the finite number of photo-electrons generated when an annihilation photon is detected gives rise to a time jitter during the rise time that adds to the uncertainty in event timing. This effect becomes more severe with detectors that have relatively low light output [13].

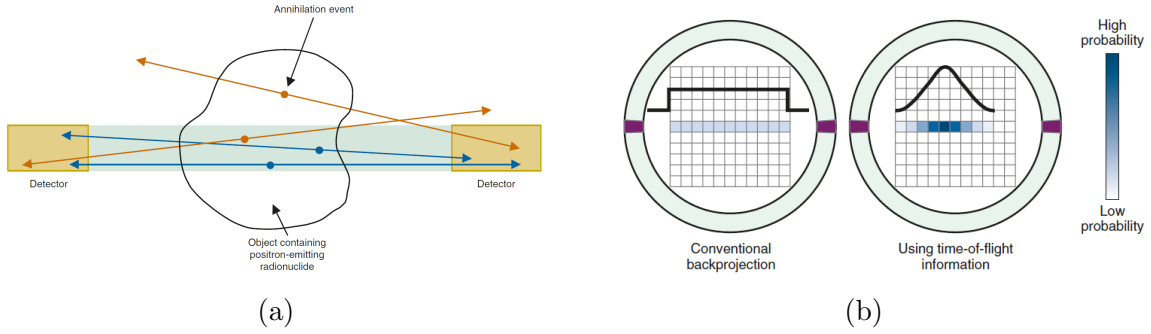


Figure 2.4: (a) The detection of 511 keV annihilation photons by two opposing detectors. The two blue lines are detected annihilation events, since the two photons are both detected. The two orange lines are non-detected events, since only one of the two photons is detected. (b) The principle of TOF-PET to trace back the position of the annihilation event along the LOR. [13].

In-beam PET

In-beam PET refers to PET detectors integrated into the beam delivery system of proton therapy. The most important advantage of in-beam detectors is the time course of PET acquisitions. To minimize the delay between treatment and PET acquisition, it can be started immediately following the irradiation treatment in order to lose as less activity as possible. Disadvantages of dedicated PET systems integrated into the beam delivery system are the costs and complex technical demands.

2.2.1 Ionizing radiation - Interaction of electromagnetic radiation with matter.

In order to understand how the photons are detected in a PET system, we will have a look into the interaction mechanisms of photons with matter. Since we are looking at the interaction with single atoms, the electromagnetic radiation can be approached as packets of energy called photons that behave as if they are particles instead of using the classical wave theory. The transfer of energy of high energy photons with atoms, nuclei and electrons occurs with complex interactions, which in the end can basically be seen as a collision between a photon and its target (nuclei or electron). There are in total nine possible interaction mechanisms, but only three are relevant and important. Those are the photoelectric effect, Compton scattering, and pair production [8].

In the photoelectric effect the energy of the photon is totally absorbed by the target atom and one of its electrons is ejected from its orbital. This so called photoelectron has an energy that is equal to the difference between the photon energy and the electron binding energy. Compton scattering is a collision between a photon and a "nearly-free" electron, because the photon has much higher energy than the electron. This results in knocking-out the electron out of the atom and scattering of the photon. In the

last interaction type, pair production, the incoming photon energy is used to produce a positron-electron pair. Which one of these interactions occur depends both on the energy of the photon and on the atomic number of the matter it traverses. Figure 2.5 shows the well-known graph of the three interaction mechanisms, and at which photon energy and atomic number combination which mechanism is dominant.

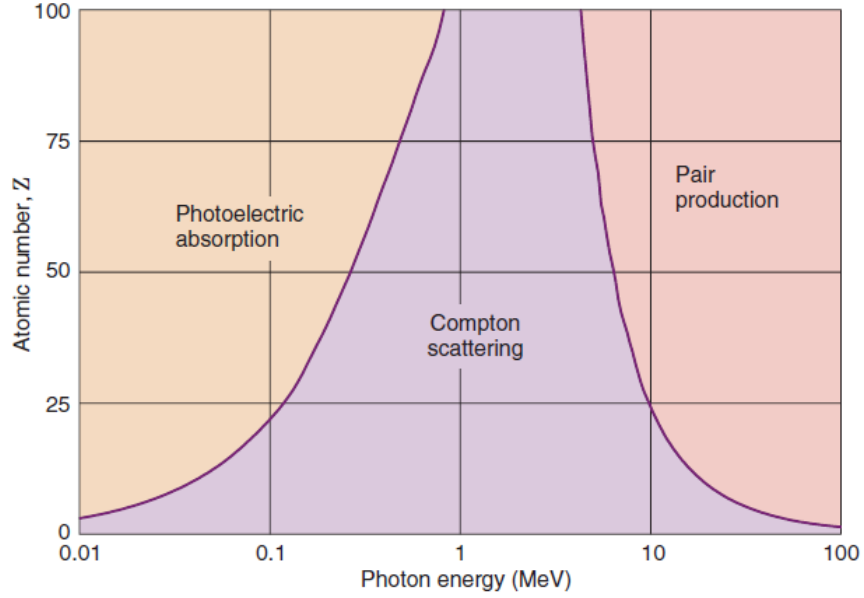


Figure 2.5: Dominating photon interaction mechanisms as a function of photon energy and atomic number of the matter that the photon traverses [8].

2.2.2 PET detectors

PET detectors basically consists of two main parts, a scintillation crystal and an array of photosensors. By now, a variety of different photosensors are available in PET scanners to detect annihilation photons, for example the photomultiplier tube (PMT). As should be clear from the previous theory, in PET there should always be used two opposing detectors. It is quite difficult to detect the 511 keV annihilation photons directly. Instead, a scintillation crystal is used in front of the detector. This is a material that exhibits scintillation, a luminescence process whereby light of a characteristic spectrum is emitted following the absorption of radiation, where the emitted radiation is usually way less energetic than that absorbed. This scintillation crystal thus creates a lot of so called scintillation photons when hit by one 511 keV gamma-photon. These (secondary) photons are easier to detect with a variety of photodetectors. Here we highlight the single photon avalanche diode, capable of detecting single photons.

A single-photon avalanche diode (SPAD), is a solid-state photo detector in which a photon-generated carrier, electron or hole, can trigger an avalanche current due to the impact ionization mechanism. The detection of the scintillation photons generated

by 511 keV annihilation photon impinging on the crystal is done by the SPAD's, also called Geiger-mode avalanche photo diodes, G-APD. These are very small semiconductor devices capable of detecting single photons and low intensity signals and record the energy and time of arrival, with very high temporal resolution of up to ten picoseconds, of the incoming photons. A typical electronic circuitry of such a SPAD is shown in figure 2.6

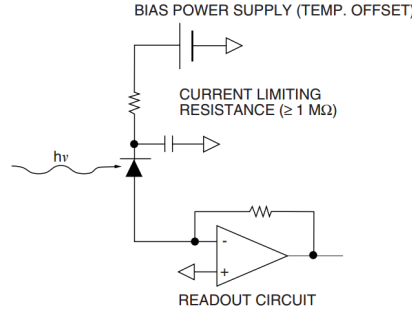


Figure 2.6: Typical circuitry of an SPAD where, along with the pn-diode where the photon hits, the power supply, current limiting resistance and readout circuit is shown.

SPAD cells are semiconductor devices based on a p-n junction reversed biased at a voltage higher than the breakdown voltage. This is the main difference between an APD, which are operating slightly below the breakdown voltage of the p-n junction. A p-n junction is a type of semiconductor device where a sharp interface exists of a positively doped side, the p-side, and a negatively doped side, the n-side. At this interface, electrons from the n region near the p-n interface tend to diffuse into the p region leaving behind positively charged ions in the n region and being recombined with holes, forming negatively charged ions in the p region. Likewise, holes from the p-type region near the p-n interface begin to diffuse into the n-type region, leaving behind negatively charged ions in the p region and recombining with electrons, forming positive ions in the n region. The resulting effect is that there is a built-in potential being created at the p-n interface, also known as the depletion zone. Figure 2.7a shows a standard pn junction and the created depletion region. Figure 2.7b shows how a pn junction is used to create a SPAD.

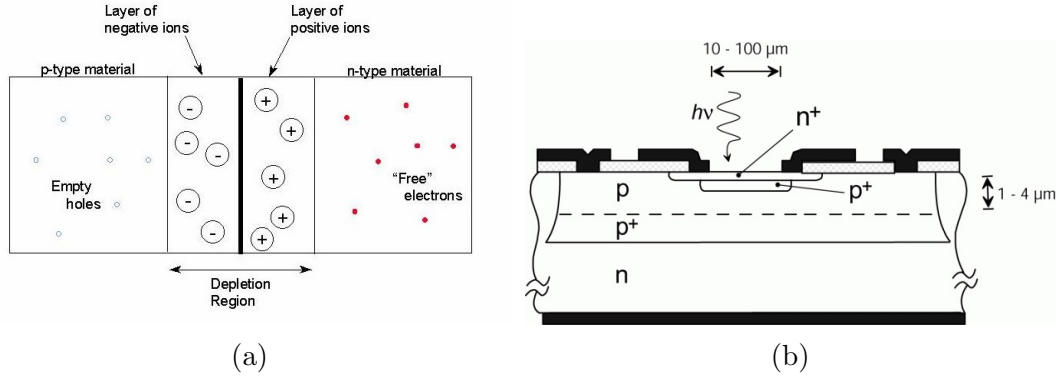


Figure 2.7: (a) A standard pn-junction. Left is the p-doped material and right is the n-doped material. In the middle the created depletion region can be seen and why there is a built-in potential. (b) The side view of a SPAD. The top layer is the actual pn-junction where a photon with energy $h\nu$ strikes in order to create an avalanche.

A p-n diode has an energy band diagram as shown in figure 2.8a, and has, under an applied voltage, a current vs. voltage, I-V, characteristics shown in figure 2.8b. It can be seen that there are three regions of the IV curve. First, there is a forward region, in which the applied potential is larger than the junction's built-in potential, allowing the flow of a current. Then there is a reverse region, in which very little current is able to flow, but the electric field magnitude in the junction increases with the applied potential. At last there is the breakdown region. Here the applied potential is so large that the pn-potential will give in and allow current to flow in the reverse direction. This breakdown region is essential for single photon detection [9].

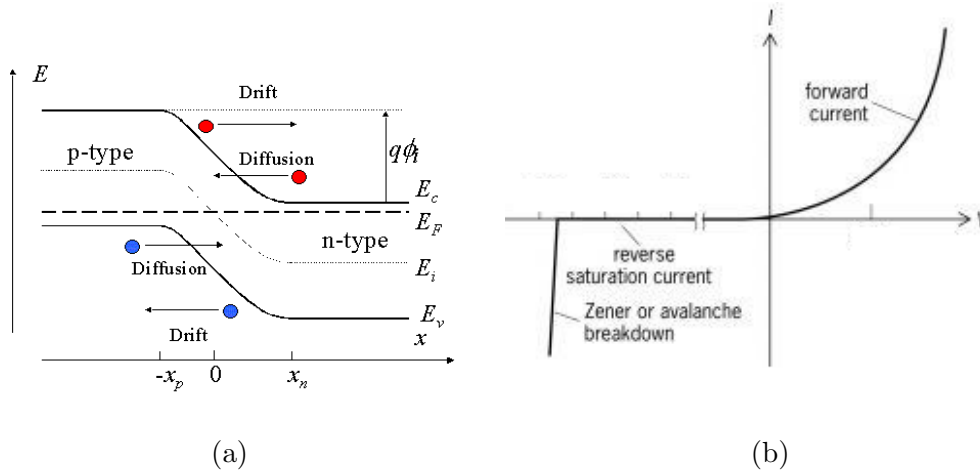


Figure 2.8: (a) Shows the energy band diagram of a p-n junction and (b) shows the current-voltage characteristics of a pn-junction.

In a pn-junction charge is carried by both electrons and electron holes. When there is excitation happening of an atom in the diode, an electron/hole pair will be created and, due to the potential of the diode electrons will move towards the positive voltage while the holes will move towards the negative voltage and so creating a current. This excitation can, for example, be due to an incoming photon. When the applied voltage over the diode is in the breakdown region, the mobile electron and/or hole may be accelerated to high enough speeds to knock other bound electrons free, creating more free-electron-hole pairs, which means more charge carriers, increasing the current and leading to further "knocking out" processes and creating an avalanche. Therefore, when only one single incoming photon creates only one electron/hole pair, the avalanche principle creates a current high enough to detect and distinguish from electronic noise. Due to this internal gain mechanism, these detector elements are useful to detect single photons.

One of the most important properties of single photon detectors is the photon detection efficiency (PDE). Another quantity is the quantum efficiency (QE) which is mostly dependent on the material properties, it refers to probability of the conversion of a photon into an electron-hole pair. The photon detection efficiency is, on the other hand, hardly dependent on the operating conditions, like temperature and applied voltage, and refers to the probability that the detector generates a digital output pulse corresponding to an incoming single photon. The PDE also depends on the wavelength of the photon, and in figure 2.9 a graph is shown of the PDE as a function of photon wavelength [14].

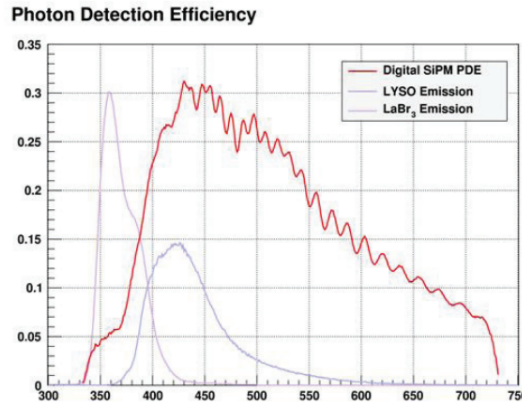


Figure 2.9: The Photon Detection Efficiency as a function of wavelength (red). Also, the emission spectra of the LYSO crystal is plotted (blue) [14], along with that of LaBr3 (light-red).

Chapter 3

Experimental Setup

This chapter discusses the detector module details, and describes the different experiments that have been done. First, the geometrical configuration of the detectors is explained, followed by the principle of operation of the detector modules. Then, the setup of the different experiments is discussed.

3.1 Materials

3.1.1 Philips Digital Photon Counting detectors

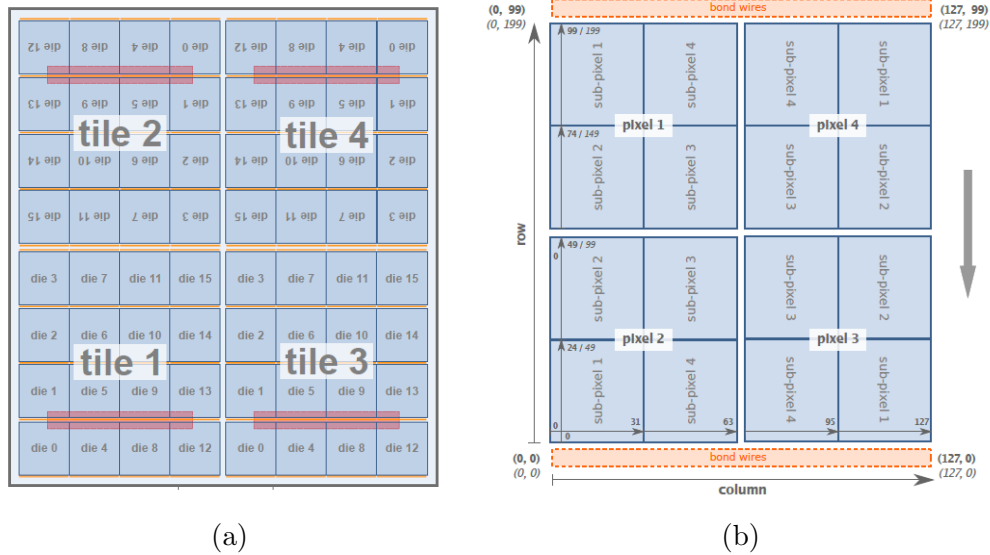


Figure 3.1: (a) A schematic front view of the module sensor, divided into tiles and dies. (b) A schematic front view of a die, divided into pixels and sub-pixels.

The module sensor used in the experiments was DPC3200-22-44-M22 (Module-TEK version) made by Philips digital photon counting (PDPC), covered with a 22mm thick LYSO scintillation crystal, together forming one detector with a total surface area of about 66 mm by 66 mm. One module sensor consists of a 2 by 2 matrix of DPC3200-2244 tile sensors, which in turn consist of 16 individual DPCxx00-22 sensor dies arranged in a 4 by 4 matrix. One sensor die is made up of 4 pixels arranged in a 2 by 2 matrix and they are each further divided into four sub-pixels. Figure 3.1a shows the front view of the layout of the sensor. Here it is clear how the detector is divided into tiles and dies. A DPCxx00-22 die layout front view is shown in figure 3.1b, which shows the pixels and the sub-pixel arrangement of a single die. So one detector consists of 256 pixel elements. Every pixel contains 3200 Geiger-mode cells, or SPAD cells, discussed thoroughly in the previous chapter, which perform the actual photon detection of the scintillation photons generated by the LYSO crystal which is in front of the modules. Some words about this LYSO scintillation crystal come later in the text when its radioactivity is discussed.

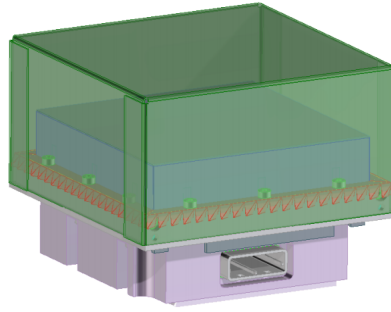


Figure 3.2: 3-D view of the DPC3200-22-44-M22 detector module with aluminum housing cover

Figure 3.2 shows a three dimensional schematic of the detector. On top is the aluminum housing that has been designed for good heat transport from the tile sensors to the housing surface, which allows to construct an efficient temperature stabilization system for the photon counting sensors when cooling the module sensor.

The detector modules are cooled using a combination of Peltier elements and a heat exchange plate with a cooled flow of ethanol in order to minimize the sensor dark-count rate (DCR). The temperature at which the measurements were done was ranging from 5 °C to 6 °C. The modules were held in a dark low-light box positioned facing each other on an optical platform to ensure perfect alignment, and each detector was surrounded by a black box of styrofoam for further light protection and temperature stability. In order to prevent condensation of moisture on the detectors, because of cooling, a slight continuous flow of nitrogen gas was provided inside of the box of styrofoam. Everything was then connected to a base unit and a laptop to control and operate the setup. The whole experimental setup is shown in figure 3.3a

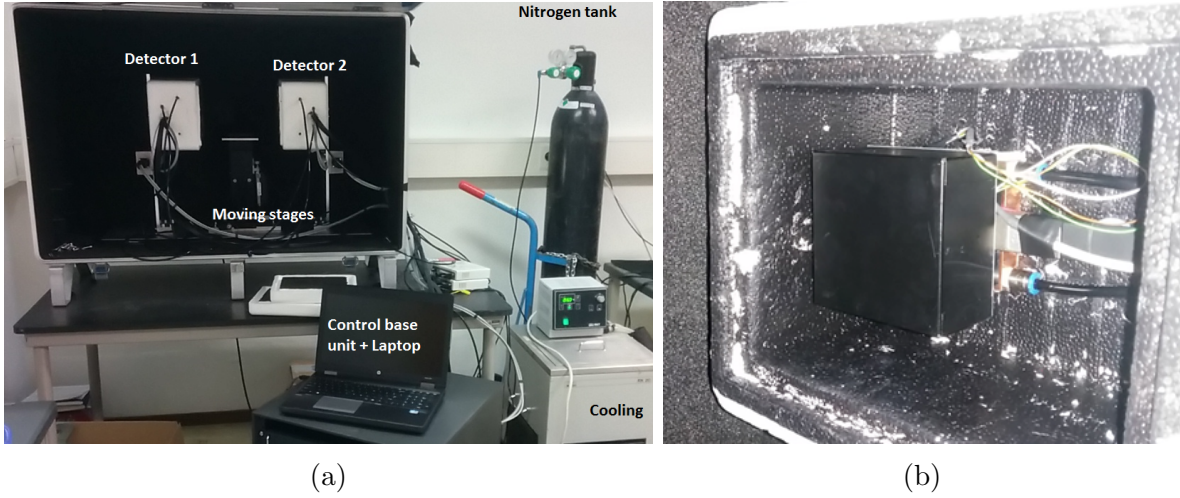


Figure 3.3: (a) Picture of the experimental setup. Both detectors surrounded by styro-foam can be seen placed inside a low-light box that can be closed. Furthermore there is the cooling system, nitrogen tank and the control base unit with laptop. (b) A close up of one of the detectors.

3.1.2 Detector operation

Now that the geometrical details of the detector have been discussed, the text continues with the operation of the detectors. It will be clear how the data looks like and more importantly, how it is being produced by the detection of a photon. A detailed description of the experimental procedure is given in Appendix A.

Event Acquisition

The detector sensor dies are collecting data with an event-based acquisition sequence and are working independently from each other. This event acquisition sequence is waiting in a ready state, and is started when a trigger occurs, which will be explained later. After the trigger there is a validation of the event, which has either yes or no as an output. If it is no, the event is not valid and all the SPAD cells of the die are being recharged into the ready state. If the output of the validation is yes, then the event will be integrated and the readout into real data is performed which completes the event. Then the die is recharged into the ready state waiting for the next trigger.

Trigger

In the most simple case a trigger is just one photon, which starts the acquisition when detected by one of the die pixels. The trigger also defines when the event timestamp is generated. However, it is possible to set a certain trigger logic to suppress dark-count noise events. This trigger logic is acting on the sub-pixel level, where these sub-pixels are connected to each other via logic gates, and there are four trigger schemes that can

be set. The first one is just when one of the sub-pixels detects a photon, or cell discharge. The second and third one have both two sub-pixel charges needed for a trigger, and the last one needs all sub-pixels to detect a photon to generate the trigger. There is an average photon count threshold corresponding to each of these trigger schemes. The different schemes and their thresholds are shown in figure 3.4.

Trigger Scheme	Sub-Pixel Configuration	Average Threshold
1	$sp1 \vee sp2 \vee sp3 \vee sp4$	1.0
2	$[(sp1 \vee sp2) \wedge (sp3 \vee sp4)]$ \vee $[(sp1 \vee sp4) \wedge (sp2 \vee sp3)]$	2.33 (± 0.67)
3	$(sp1 \vee sp2) \wedge (sp3 \vee sp4)$	3.0 (± 1.4)
4	$sp1 \wedge sp2 \wedge sp3 \wedge sp4$	8.3 (± 3.8)

Figure 3.4: Different trigger scheme possibilities including the average photon count threshold. The \wedge symbols corresponds to an AND operation and the \vee symbol corresponds to an OR operation.

Validation

The validation stage is a second threshold to separate real annihilation photon events from dark counts of the micro-cells. As the trigger stage, it too is a logic operation, but now on the scale of the distribution of SPAD cell discharges on the pixel. If the required distribution is met at the end of the validation interval, the event will be validated. This is an extra way to correct for dark-count noise events.

Integration

During the integration interval the sensor waits for more scintillation photons from the corresponding annihilation event. This phase should take long enough to collect all delayed photons from the decay of crystal scintillation.

Readout

The readout of the sensor starts after the integration phase. It reads the state of the micro-cells row by row, and the processed rows are already recharged during this phase. Cell discharges, e.g. delayed scintillation photons or dark counts, that happen during the readout phase are still counted, as long as they occur in cell rows that have not been read and recharged.

Data output

Figure 3.5 shows an example of a output data file. Each row corresponds to one event, or detected photon, where the complete validation scheme is completed. The first column indicates at which detector the event happened. The second and third columns indicate the tile number and die number respectively. The data is ordered in certain frames, which number is shown in column four, and within one frame, each event gets a certain time stamp depicted in the fifth column. Then column six till nine shows the measured number of scintillation photons for every pixel on the corresponding die. The last columns indicates the temperature of the corresponding tile.

#> bb,	tile,	die,	frame_nr,	timestamp,	p1,	p2,	p3,	p4,	temp,
1,	2,	3,	11532,	2777892,	689,	112,	41,	182,	4.94,
1,	2,	9,	11532,	4175759,	194,	60,	132,	982,	4.94,
1,	1,	15,	11532,	4208970,	158,	81,	184,	897,	4.88,
1,	3,	2,	11532,	14396905,	181,	1100,	765,	143,	5.00,
2,	1,	12,	11532,	3008965,	46,	157,	1199,	122,	6.12,
2,	1,	7,	11532,	8274188,	111,	340,	826,	215,	6.12,
2,	4,	9,	11532,	8846673,	41,	98,	1014,	220,	6.19,
2,	3,	12,	11532,	11486122,	82,	232,	1001,	177,	6.12,

Figure 3.5: Example of the data output of the detectors.

3.2 Experimental methods

3.2.1 Detector efficiency

The efficiency of the detectors was measured as a function of the position of the ^{22}Na source within a plane perpendicular to the detector faces. This plane lies exactly at the midpoint between the two detectors. The source was scanned over one quarter of the plane, with steps of 6.5 mm in both directions (x and y), resulting in a total of $6 \times 6 = 36$ measurement points. Due to symmetry, only one quarter, corresponding one tile of the sensor, was measured to represent the whole detector. At each position data was collected for about 11 minutes, and all coincidences within a 10 ns time window were taken into account. The efficiency for each position of the ^{22}Na with an activity of 387 kBq was then calculated by

$$\text{Efficiency}(\%) = \frac{\text{number of coincidences}}{387 \times 10^3 \text{Bq}(s^{-1}) \times \text{time}(s)} \times 100\%. \quad (3.1)$$

3.2.2 Time skew correction

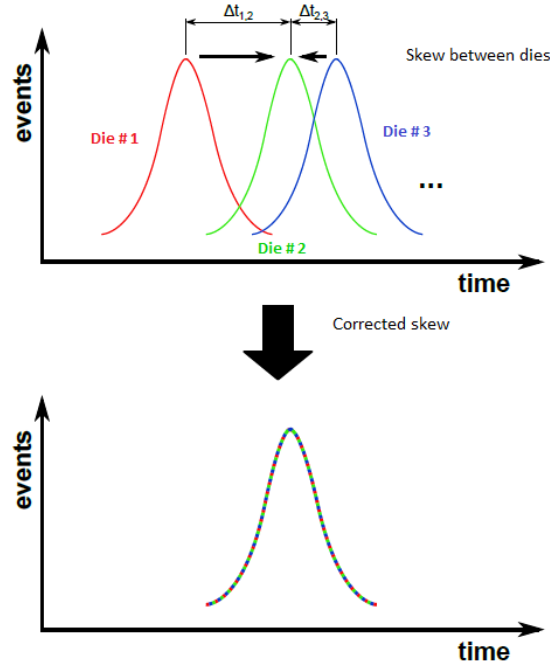


Figure 3.6: Time skew correction between two dies with one selected reference die, in the figure referred to as die # 2. The reference die is often chosen as the die with the lowest time skew.

An important goal of a sensor development aiming at high timing accuracy for TOF-PET applications is to achieve a good timing resolution across larger sensor arrays. Because of small signal runtime differences between individual dies and tiles in the measurement setup, the individual dies see their TDC reference clock with a small individual offset, or skew, and eventually the recorded or generated timestamp value for that die has the same offset. Correcting for these electronic time skews between the DPC dies is of utmost importance for obtaining good timing performance. Figure 3.6 shows a schematic explanation of this timestamp skew correction.

In the original manual of the Philips digital photon counting detector modules, the time skew correction measurements are proposed to be performed with an direct approach for determining the time skews by irradiating the entire DPC-array simultaneously with a pulsed laser. However, in this research a different approach was used, based on a method proposed by Lopes et al [16]. With this indirect approach it is possible to use the ^{22}Na and performing coincidence measurements. Then the skews can be measured for each die combination of both detectors. This timing calibration basically consists of three steps:

- i) Two coincidence measurements were done, with the ^{22}Na source placed in the midpoint on the aluminum housing of detector 1 in the first measurement, and in

the second measurement the source was placed in the midpoint on the aluminum housing of detector 2. In this way, since the source is placed in the midpoint very close to one of the detectors, the four central dies, each corresponding to a different tile, will collect most of the events, whereas on the opposing detector all dies will collect events. Because of geometry, each one of these four central reference dies of the detector with the source nearby will collect coincidences with all dies on one of the opposing detector's tiles. This tile will be the diagonally opposing tile. By looking at figure 3.1a we see that these central reference dies are die 15 of tile 1, die 3 of tile 2 and 3, and die 15 of tile 4.

- ii) By plotting the histograms of the timestamp difference of all coincidences between each of the four central reference dies with the corresponding dies of the diagonally opposing tiles, we know the timestamp skew values between all dies of a certain tile on the detector far away from the source. The same will be done when the source is placed on the other detector and then we will know the timestamp skew values between all dies on a certain tile for both detectors.
- iii) Now we have to determine the timestamp skew values between each of the four central reference dies for both detectors. This will be done by selecting coincidences between an arbitrary central reference die of one detector and all four central reference dies of the opposing detectors. By doing this for both detectors we not only know the timestamp skews between the four central reference dies for both detectors, but between all dies on a certain detector.
- iv) What remains to be done is to determine the timestamp skew values for all die combinations between both detectors have to be calculated. This will be done by first calculating the skews of the combination of all four central reference dies with their diagonally opposed central reference die, by adding the peak positions of the timestamp difference histograms of a certain reference die combination from both measurements created earlier in step ii) to eliminate the time-of-flight, ΔToF , part of the timestamp difference value. An detailed explanation of this time skew correction method is given in Appendix B.

3.2.3 High count rate performance

When too much photons reach the detector in a too small time interval, the sensor will get saturated and problems can occur in the data processing of the detector. So, for higher photon count values, saturation effects start to play a bigger role. For example, a lot of photons will not be detected because the acquisition system is still busy processing the previous events. This leads to a pile-up of photon counts. Also, it can happen that two events coming very fast after each other, within the recharge time of the detector, these events will be counted as one simultaneous event, eventually giving a wrong photon count number, thus a wrong photon energy value.

To investigate these possible issues, experiments at different count rates should be performed. Since experiments were done only with one source, the radioactive ^{22}Na isotope with a fixed activity, it was not possible to alter the source activity. However, to alter the count rate for one detector only, the source was placed closer to the detector. In total three positions are considered for both detectors: in the center of the two detectors, corresponding to an distance of 16 cm, at a distance of about 2.6 cm from the detector and on the aluminum housing of the detector, which is roughly 0.1 cm away from the detector. For every position the time the source was facing the detector exactly at its midpoint ¹.

In order to get an estimation on how much photons annihilation photons will hit one detector, we use some geometric calculations. First, for simplification, we assume that we have a circular detector instead of a square one. The radius of this circular detector is such that the area is equal to the area of the original square detector. Let x be the distance of the source to the midpoint of the detector and let r_d be the radius of the circular detector. Since the area of the detector is $66 \text{ mm} \times 66 \text{ mm} = 4.4 \text{ cm}^2$, the radius should be

$$r_d = \sqrt{\frac{A}{4\pi}}.$$

Imagine a sphere with the source at its midpoint and its radius r_s is the distance from the source to the edge of the detector, and the angle θ is the angle between this radius and x :

$$r_s = \sqrt{x^2 + 2d^2}$$

$$\theta = \tan^{-1}\left(\frac{r_d}{x}\right).$$

The surface area of the cap of the sphere behind the detector (the shadow of the detector on the sphere) is given by

$$A_{cap} = 2\pi r_s^2(1 - \cos\theta).$$

Figure 3.7 shows a schematic representation of the above. The gray part of the sphere is the area A_{cap} . From the figure it is also clear that the radius of the sphere depends on the source distance.

¹This midpoint was found by performing short measurements after each other, each time changing the position very slightly. Because of geometry the midpoint was taken to be the position at which the detector recorded the most events.

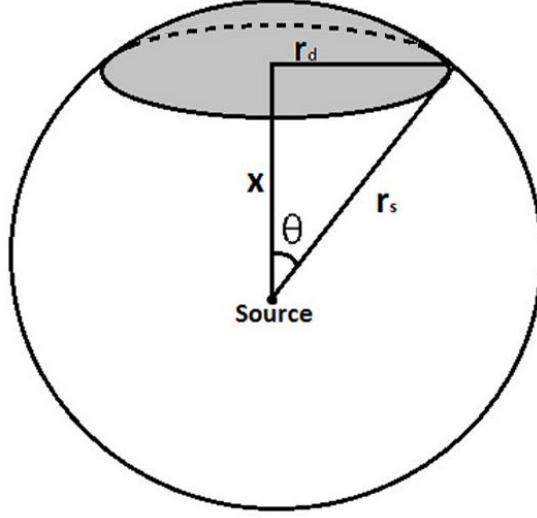


Figure 3.7: Schematic of the area of a cap of a sphere when using a circular detector with radius r_d and a source at distance x .

Because the source emits the annihilation photons randomly in all directions, the fraction that will hit the detector can easily be calculated by dividing the surface area of the cap of the sphere behind the detector, A_{cap} by the total surface area of the sphere with, times 2 times² the activity of the source, $R_{22\text{Na}}$:

$$\begin{aligned} R_{\text{photon}}(x) &= \frac{2\pi r_s^2(1 - \cos\theta)}{4\pi r_s^2} \times 2R_{22\text{Na}} \\ &= (1 - \cos\theta) \times R_{22\text{Na}}, \end{aligned} \quad (3.2)$$

So when the source is placed on the aluminum housing of the detector, θ will go to 90 degrees and R will become equal to $R_{22\text{Na}}$. All photon rate values are given in table 3.1.

Source distance, x (mm)	Photon rate $\times 10^6$, R_{photon} (s^{-1})
161	0.044 ± 0.001
26	0.152 ± 0.005
1	0.378 ± 0.012

Table 3.1: The 511 keV photon rate that the detector mathematically should be detecting for different source positions.

²Because the source emits two annihilation photons in opposite direction.

3.2.4 Intrinsic radioactivity

The detector molecules make use of a lutetium based scintillator, LBS, to convert the incoming 511 keV gamma rays into photons of energy within the detection range of the SPAD cells. The annihilation photons deposit their energy in the scintillators and generate optical photons which can be detected by the optical photon detectors. There are a variety of different scintillation crystals, such as NaI(Tl) or BGO, that can be used and have been used in other detectors. The reason to use a lutetium based scintillator (LBS) for PET is their high stopping power for 511 keV, high light yield and, especially important for TOF-PET, their short decay time. Also, looking at the photon detection efficiency plot of the SPAD cells in figure 2.9, the peak of the photon detection efficiency corresponds more or less with the peak of the LYSO emission intensity vs wavelength plot.

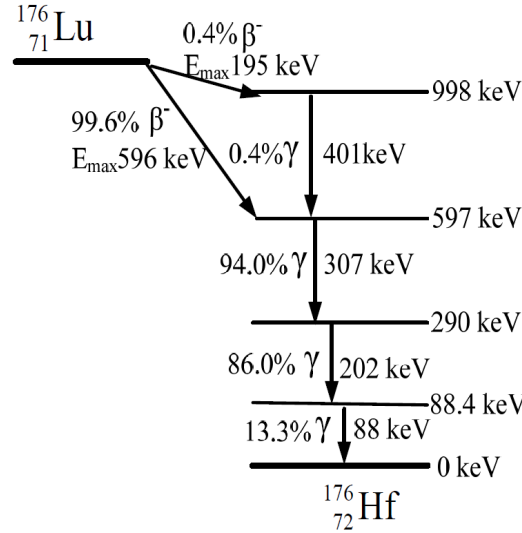


Figure 3.8: Decay scheme of ^{176}Lu [17].

Lutetium is an element with atomic number 71, and has a radioactive isotope, ^{176}Lu , which is relatively abundant (2.6 %). This long-lived radioactive element has a half-life of about 36 billion years and its decay scheme is shown in figure 3.8. The main process of ^{176}Lu to ^{176}Hf is a β -particle emission, with a maximum energy of 596 keV, and three simultaneous gamma-ray emissions, with energies of 88, 202 and 307 keV [17]. The count rate of a milliliter scintillator can be calculated with

$$R = \frac{n\rho N_a}{M} * 0.026 * (1 - e^{-0.693/T_{1/2}}) \quad (3.3)$$

$$\approx \frac{n\rho N_A}{M} * 0.026 * \frac{0.693}{T_{1/2}}, \quad (3.4)$$

where n is the subscript number of Lu in the scintillator molecular formula, ρ is the density, N_A is Avogadro's constant (6.02×10^{23}) and M is the molar mass. From

section 3.1 we know the dimensions of the LYSO scintillation crystal and from that its volume can be calculated to be about $96 \times 10^3 \text{ mm}^3 = 96 \text{ ml}$ of scintillation material. Now from equation 3.4 the count rate of 1 ml LYSO scintillation crystal, with molecular formula $\text{Lu}_{1.8}\text{Y}_{0.2}\text{SiO}_5$, can be calculated to be about 288 Bq, where $n = 1.8$, $\rho = 7.4 \text{ g/cm}^3$ and $M = 442.6$ [18]. Multiplying this activity of 1 ml LYSO scintillation crystal with its total volume, we get a total intrinsic count rate of the LYSO scintillation crystal for one detector, R_{LYSO} , to be about 27.6 kBq.

The activity of this radioactive isotope of the scintillation crystal is high enough to be taken into account for generating false photon counts by the detectors. The β^- particles emitted by the decay deposit energies mostly in the same LBS crystal due to the short range of these particles. The gamma-rays, however, can be detected not only in the same LBS crystal, but also in the opposing LBS crystal by emitting outside the original crystal.

The intrinsic radiation of the scintillation crystals, and thus the detectors, is being investigated with the aid of blank measurement, that is, without a source. Here the detectors are placed as close as possible to each other to capture as much as possible intrinsic coincidences. We will look at how the intrinsic radiation of ^{176}Lu affects the energy histogram plot (e.g. the energy resolution), and the timing resolution.

Chapter 4

Results

4.1 Detector efficiency

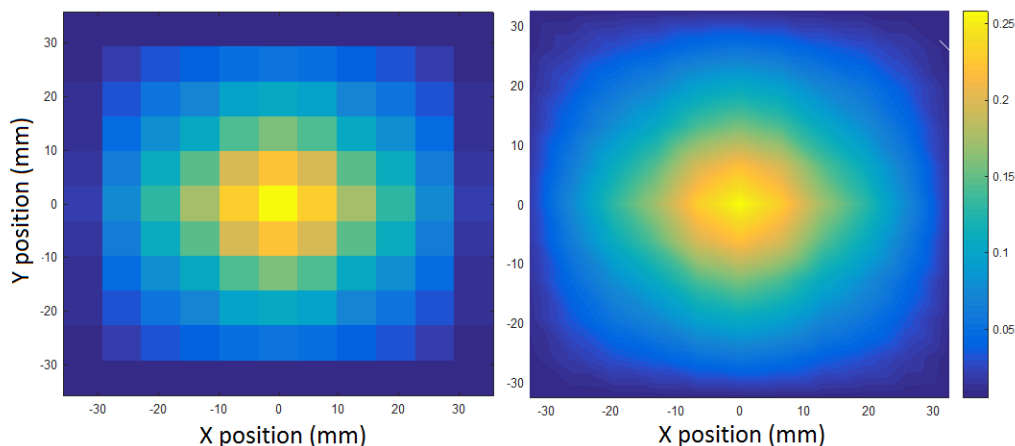


Figure 4.1: Detector efficiency (%) as a function of source position on a plane at the midpoint between the two detectors. Left shows the discrete efficiency values corresponding to each source position and right shows the interpolated map.

Figure 4.1 shows the 2-D map of the efficiency of the detectors as a function of the ^{22}Na source position with the source lying in the plane in the middle of and perpendicular to the two detectors. The results are based on coincidence events within a time window of 10 ns and an energy window of 350 to 650 keV. The left map is the plot of the discrete efficiency values corresponding to each source position, and the right map is the interpolated plot. The maximum efficiency, as would be expected, is obtained when the source is positioned exactly at the midpoint. This maximum is slightly above

0.25 percent. The efficiency drops towards zero when the source is placed towards the edges of the detectors, which makes sense because any further it is geometrically not possible to detect photons from the annihilation events of the source in coincidence since at least one of the two photons will not hit a detector.

4.2 Time skew correction

Figure 4.2 shows the timestamp skew values in picoseconds of all dies for both detectors obtained in the time skew correction measurements (step i) and ii)). The values correspond to the die numbers shown in figure 3.1a. For both detectors there is an additional graph of these time skew values as a function of die number for each tile plotted. What can be seen from these graphs is that, when comparing the two detectors, the time skews of their dies are more or less the same for all tiles, since they show the same trend. When comparing the tiles, there is a large time skew between them, up to almost 1.2 ns.

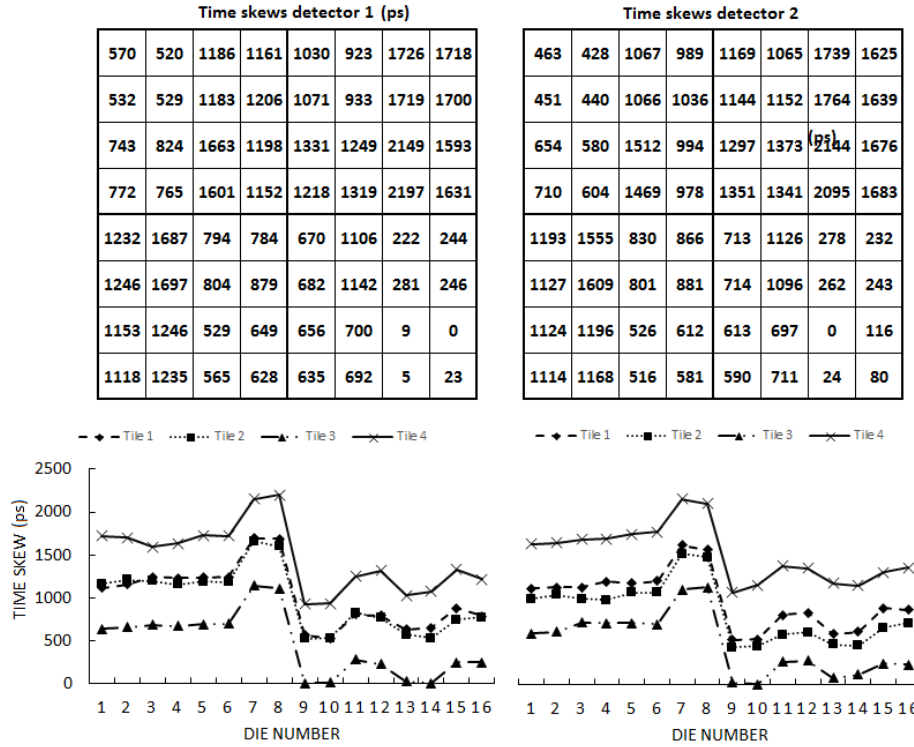


Figure 4.2: Timestamp skew in picoseconds of all dies for both detectors. For each detector one die is selected to be the 'zero-skew'. Graphs of the time skews as a function of die number for all four tiles on both detectors are added.

Figure 4.3 shows the effect of time skew correction on the timing resolution for coincidence measurements. The graphs shows histogram plots of timestamp differences and

corrected timestamp differences of the coincidence events obtained from the measurement with the ^{22}Na source placed on detector 2. Without the correction the FWHM of the time difference, dt , histogram plot is about 1.704 ns and after correcting for the time skews, the FWHM is about 1.095 ns, which means that the time resolution improves by almost 36%.

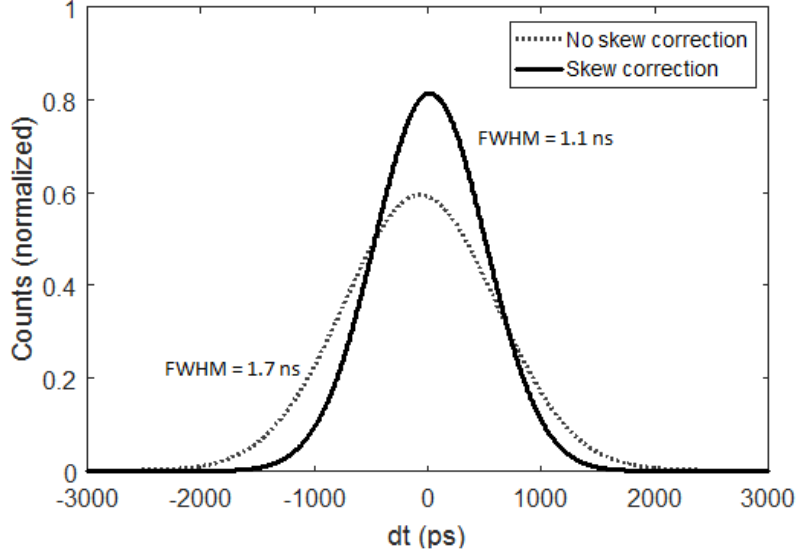


Figure 4.3: Histogram plot of time differences for coincidence events with and without time skew correction of the dies.

4.3 High count rate performance

Table 4.1 gives the count rate and photon rate values as a function of the source distance from the detector. Figure 4.4 shows a graph of the number of detected events per second for the three measured points. The data points show an $(1-\cos\theta) + C$ relationship of the count rate with increasing distance of the source away from the detector, where C is a constant that represents the background photon rate, which is 0.023 s^{-1} . This number corresponds quite well with the intrinsic activity of the LYSO crystal calculated in section 3.2.4. When the source is getting closer to the detector, the data deviates somewhat from the plot goes, where a lower photon count, of about 0.13 million events per second, is measured than expected. This part is referred to as pile-up or saturation of the 511 keV photon events in either the scintillator or photodetector. .

Source distance, x (mm)	Photon rate $\times 10^6$ (s ⁻¹)	Detection rate $\times 10^6$ (s ⁻¹)
161	0.044 ± 0.001	0.021 ± 0.001
26	0.152 ± 0.005	0.049 ± 0.003
1	0.378 ± 0.012	0.133 ± 0.006

Table 4.1: The 511 keV photon rate that the detector mathematically should be detecting and the detected photon rate for different source positions.

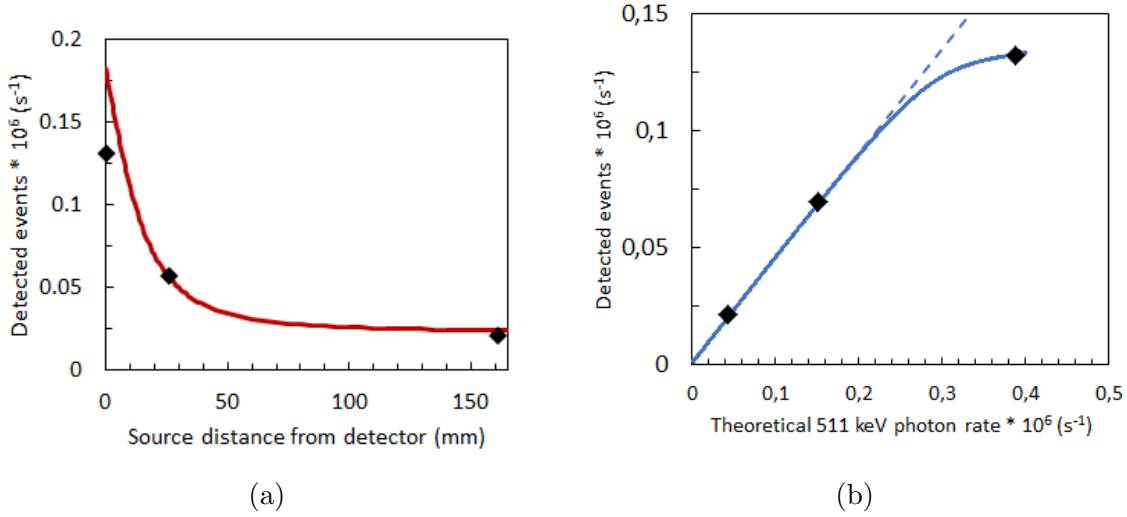


Figure 4.4: (a) Event count rate in million events per seconds as a function of source position from the detector. Dashed line is a x^{-2} relationship and the solid blue line follows that relationship except very near the detector where pile up of events or saturation occurs. (b) Event count rate in million events per seconds as a function of theoretical 511 keV annihilation photon rate.

4.3.1 Effect on timing and energy resolution

Let's have a look what effect the increase in count rate has on the timing resolution and energy resolution of the coincidence events. This will be done by making histogram plots of the time difference values and the energy spectra for the three positions of the ²²Na source described earlier in the text. In figure 4.5 all three time spectra, plotted as normal probability density functions, of the time differences of the coincidences are plotted in a single graph. It is clear that the time resolution decreases as the source gets closer to one of the detectors.

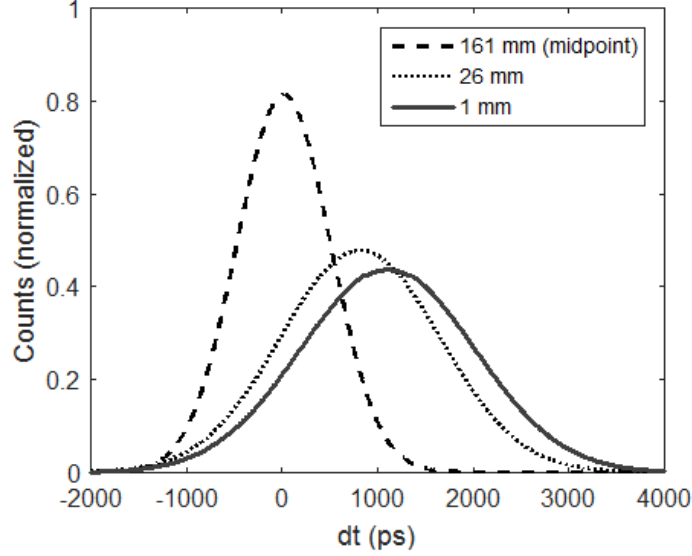


Figure 4.5: Normal probability density functions of the time differences of the coincidences for the three different source positions.

Figure 4.6 shows the three energy spectra separately corresponding to the three different source positions. The energy resolution of the 511 keV photon peak for the first two spectra are more or less the same, with FWHM of 159 and 156 keV respectively. The third spectrum has a poorer energy resolution of the 511 keV photon peak, which has a FWHM of 223 keV. What else can be seen from these spectra is that when the ^{22}Na source is placed closer towards one of the detectors, the tail of coincidence events with higher energy after the 511 keV photon peak gets bigger.

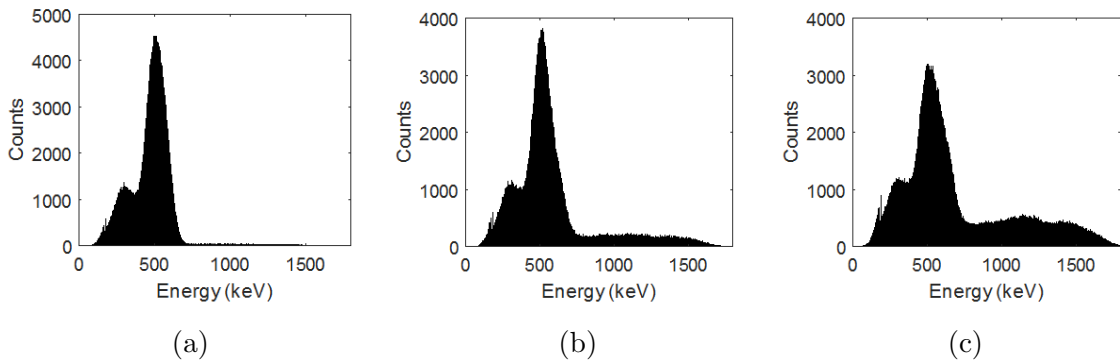


Figure 4.6: Energy spectra calibrated for the 511 keV photon peak for the three different source positions, with (a) the source at 161 mm away from the detector (midpoint), (b) the source at 26 mm away from the detector, and (c) the source at 1 mm away from the detector.

Figure 4.7 shows for both the time resolution and energy resolution as a function

of the distance of the source with respect to the midpoint between the two detectors. The FWHM values are given of the time difference histograms and 511 keV photon peak spectra to represent the time resolution and energy resolution respectively. For both the time resolution and energy resolution, placing the source further away from the midpoint, thus closer to the detector, improves the time resolution.

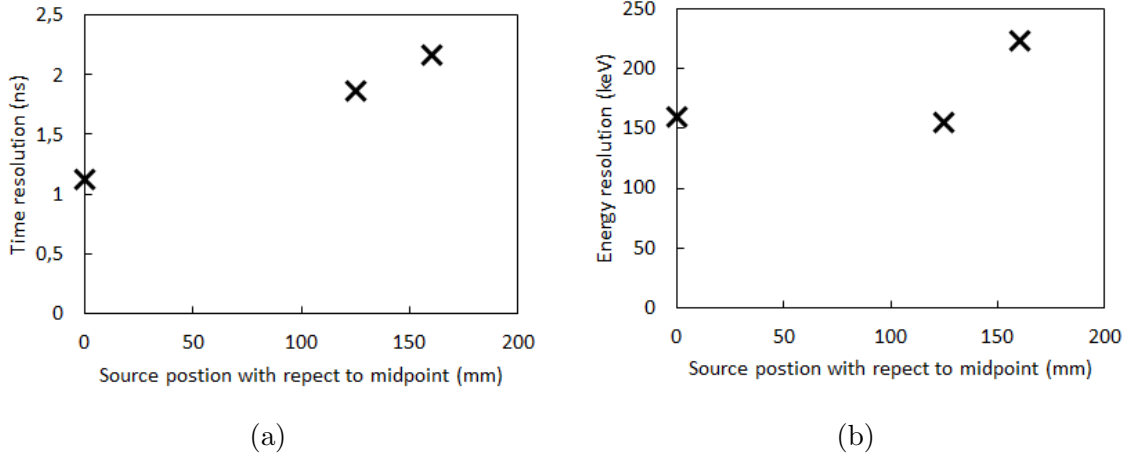


Figure 4.7: (a) Time resolution as a function of source distance. (b) Energy resolution as a function of source distance. Here it is chosen to show the source position with respect to the midpoint between the two detectors.

4.4 Intrinsic radioactivity

As mentioned before, each die gives four scintillation photon count numbers, one for each pixel on the die. These photon count values can be converted into energy of the events detected by the detectors. There are multiple ways to do this. For example only the pixel with the highest photon count will be taken, or the sum of all four pixel photon counts are converted into energy. Also, the counts of neighbouring dies may be interesting to considered. This all has to do with the spreading of the scintillation photons inside the LYSO crystal. However, it turned out that selecting the maximum value of the four photon count values is the best option, so for the rest of the results all the energy spectra are created based on the maximum photon count value per die, followed by a calibration of the 511 keV photon peak.

Figure 4.8 shows the energy spectra of coincidence events for the measurement without the source, the zero measurement, and with the source placed exactly in the midpoint between the two detectors. In the zero measurement there is a clear peak around 300 keV from the ^{176}Lu in the LYSO scintillation crystal. This peak is also visible in the coincidence energy spectra with the source in the middle, however, the 511 keV annihilation photon peak dominates the energy spectrum, as we would expect.

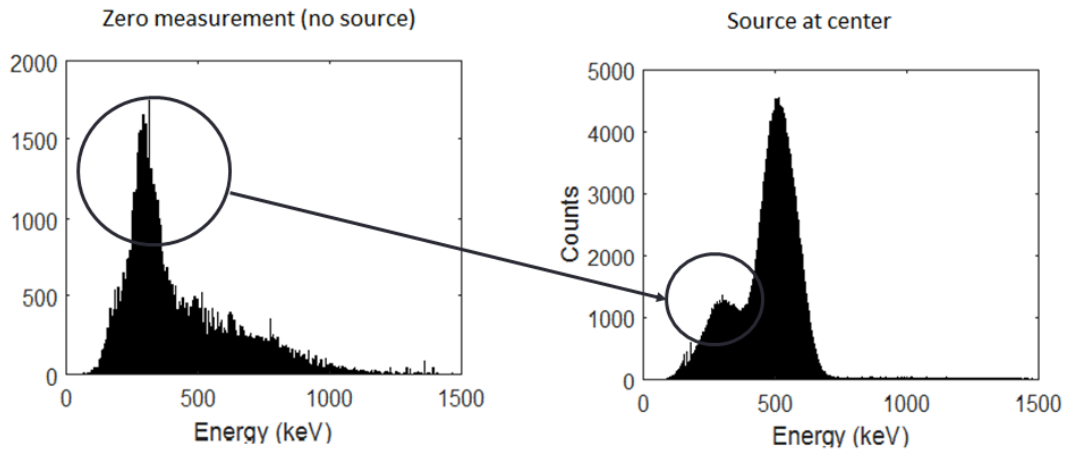


Figure 4.8: Left shows the energy spectrum of the zero measurement, with a clear peak around 300 keV, and right shows the energy spectra of the measurement with the source in the middle, where the same peak is visible but with it a way higher peak at 511 keV.

Figure 4.9 shows the energy spectrum of single events of one of the detector of a measurement with the source placed in the midpoint between the two detectors. Also here the two peaks are visible, however the energy peak at 511 keV is now way less dominant as in the energy spectrum of figure 4.8. This is because the intrinsic radioactivity of the LYSO crystal is mostly only seen in single events.

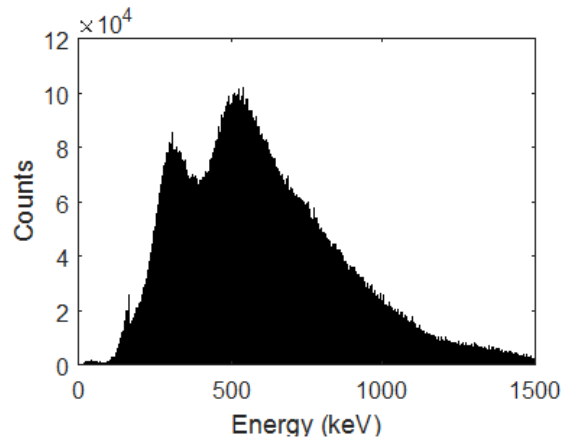


Figure 4.9

Chapter 5

Discussion and Conclusion

5.1 Detector efficiency

For the detectors efficiency as a function of source position, the data should be corrected for the fact that the detectors do not cover the whole area of annihilation photons coming from the source. These photons are randomly directed, and regarding the size of the detectors, only a small fraction of the photons will hit the detector. Equation 3.2 does give an theoretical correction for this effect. However, this equation is based on the source facing the detector at its midpoint, whereas in the measurements the lateral position of the source is being varied. So for the efficiency with the source at its midpoint, which is 0.25 %, can be corrected to be 6.2 %.

But what does this efficiency map actually tells us. We should be aware of the fact that this map represents source position and not the detector itself. It should also be considered that the efficiency map relates to coincidence events of 511 keV annihilation photons only. For other applications this efficiency map may thus not be relevant.

5.2 Time skew correction

As can be seen in figure 4.3, the time skew correction has a positive effect on the timing resolution of coincidence measurements, and consequently it will improve the spatial resolution of a TOF-PET measurement system by almost 36%. From the graphs in figure 4.2 we observe that the skews between all dies on a tile are quite similar. If we compare the four tiles, the difference between the same die numbers is more or less constant, what implies that there is also a big time skew between the tiles. For every tile we see a big difference between die 7 and 8. This is probably because the fact that these consecutive dies are placed much further apart than all the rest of the dies (see figure 3.1a). These two dies are also both on different halves of the tile.

The time skew correction method used in this research is however only suitable for

coincidence measurements. To obtain the absolute skews of all dies on a single detector, one has to precisely know the time of flight of the photons (e.g. the source position) but more importantly, the real point in time that the photon is actually sent from the source. The used method eliminates these aspects or difficulties.

5.3 High count rate performance

The data in figure 4.4a show that some sort of saturation is happening at higher count rates or if the source is placed closer to the detector. At large distances, the graph in figure 4.4a shows an $1/x$ relationship, with an offset due to the background or intrinsic activity. This can be explained by looking at the Taylor expansion of equation 3.2

$$\begin{aligned}\tan^{-1}x &= x - \frac{x^3}{3} + \frac{x^5}{5} - \frac{x^7}{7} + \dots \\ \cos x &= 1 - \frac{x^2}{2!} + \frac{x^4}{4!} - \frac{x^6}{6!} + \dots\end{aligned}$$

So, the Taylor series approximation of equation 3.2 leads to

$$1 - \cos(\tan^{-1}(d/x)) = (d/x)^2 \propto \frac{1}{x^2}. \quad (5.1)$$

However, the graph deviates in two ways from a $1/x^2$ relationship. First there is pile-up of events when the source is placed closer towards the detector. Second, the graphs shows the presence of background events, since the graphs does not tend to go to zero when x goes to infinity. This background rate is about 0.02 s^{-1} , and its main cause is the intrinsic radioactivity of the LYSO crystal.

Looking at figure 4.4b, we observe that the closer the source is placed to the detector, so the higher the 511 keV photon rate will be, the more the detection rate deviates from the theoretical expectation. This is probably caused by several factor. First it has to deal with the saturation of the photon detector elements. Also, the solid angle at which the photon hits the detector is important in this discussion, which can be seen in figure 5.1. Placing the source closer to the detector will affect the solid angle at which the photons will hit the detector for dies located more towards the edge of the detector. This will lead to a more unevenly distributed of incoming photons.

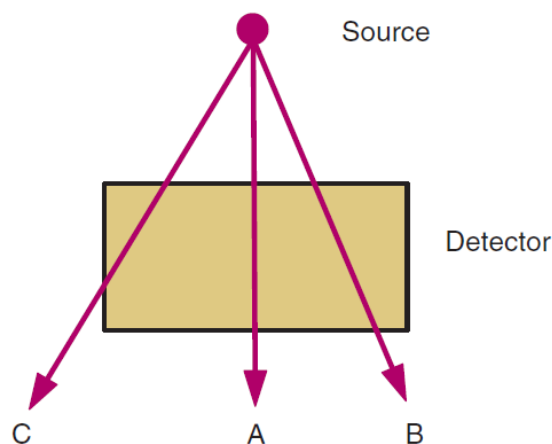


Figure 5.1: Three possible trajectories for radiations striking a detector from a point source, each having a different intrinsic detection efficiency.

Here three different trajectories are shown for photons hitting the detector. The photon of trajectory B "sees" more detector material compared with the photon of trajectory A, whereas the photon of trajectory C has a change of not even being detected, because of so called side-effects.

So both graphs in figures 4.4a and 4.4b shows some saturation phenomena. To investigate which parameter, count rate or source distance, is the main reason for this saturation we need to perform experiments with a fixed source position, but with sources of different activities, preferably higher than the current 387 kBq ^{22}Na source.

To say something more about this effect we will look at the intrinsic efficiency of the detector, ϵ , which is the ration of the detected photons by the detector over the number of photons hitting the detector. Its value is not constant over source distance, which can be seen in table 5.1. From the table it is clear that when the source is placed very close to the detector, its intrinsic efficiency decreases significantly.

Source distance, x (mm)	Intrinsic efficiency, ϵ
161	0.481
26	0.469
1	0.352

Table 5.1: The intrinsic efficiency of the detector for different source positions.

5.3.1 Effect on time and energy resolution

It turned out from figure 4.7 that the placing the source closer to the detector, and thus increasing the photon count rate, has a negative effect on the time resolution and energy resolution. The FWHM of the time difference distribution increases, so the time resolution decreases, more or less linearly when the source is place further away from

the midpoint between the two detectors. For the energy resolution, the FWHM of the 511 keV photon peak only increases when the source is very close to the detector.

One interesting thing that can be seen in these three graphs is the increase in counts after the 511 keV peak when the source is placed closer to the detector. This could be an additional explanation for the saturation phenomena described earlier, since these tails are probably caused by the fact that two events are counted as one within the time window and within the time frame of the internal clock, and adding up their energy. Another cause of these tails can be the emission of 1275 keV gamma-rays by the ^{22}Na source. Since those gamma rays are only emitted one photon per decay, instead of two perpendicular annihilation photons, they are more detected when the source is placed closer to the detector, and can cause coincidence events with other 1275 gamma-rays or even with annihilation photons.

5.4 Intrinsic radioactivity

The intrinsic radioactivity of the LYSO scintillation crystal does influence the data of the singles measurements, and after coincidence selection, its events are still present. However, since the energy of the radiation coming from this crystal is distinguishable from the 511 keV annihilation photon spectrum, selecting a proper energy window for the coincidence events will mostly filter out the events originated cause by the ^{176}Lu isotope.

From the spectra shown in figure 4.9, it is clear that by filtering out coincidence events based on a time window, already a lot of the intrinsic background counts vanishes. This is of course because these intrinsic events happen randomly, and thus a lot of the detected events between the two detectors are outside this time window and will not be counted. Furthermore, we can select an energy window around the 511 keV photon peak to filter out the events with different energy. It has been investigated what effect this will have on the time resolution, since it is expected these intrinsic coincidences do have different Δt values than the coincidences originated from the source. However, it turned out that selecting an energy window of 350 keV to 650 keV has a minimal effect on the time resolution by reducing the FWHM of the time difference histogram by about 2 picoseconds. This is probably because the time window was already sufficient narrow enough in order to filter out a relative high amount of intrinsic or random coincidences.

When we talk about intrinsic radioactivity, there are two types of intrinsic coincidences. A true coincidence is a decay event happening in the scintillation crystals of one of the detectors, which is then detected by both detectors. A random coincidence is when in both detectors scintillation crystals a decay is happening, and detected by its detector within the selected time window. This is shown in figure 5.2.



Figure 5.2: The detection of true coincidences and random coincidences caused by the intrinsic radioactivity of the LYSO crystal.

If we then look at the time histogram of the zero measurement in figure 5.3, these true and random intrinsic coincidences can be clearly seen. The two peaks represent the true intrinsic coincidences, since the distance between the two detectors are fixed, also the time differences of these coincidences should be fixed. Even the distinction can be seen of in which detector the decay happened. The random coincidences are evenly distributed over the histogram plot, since they happen random within the time window their time difference can be any value. The positions of the peaks of the true coincidences can however influence the time resolution.

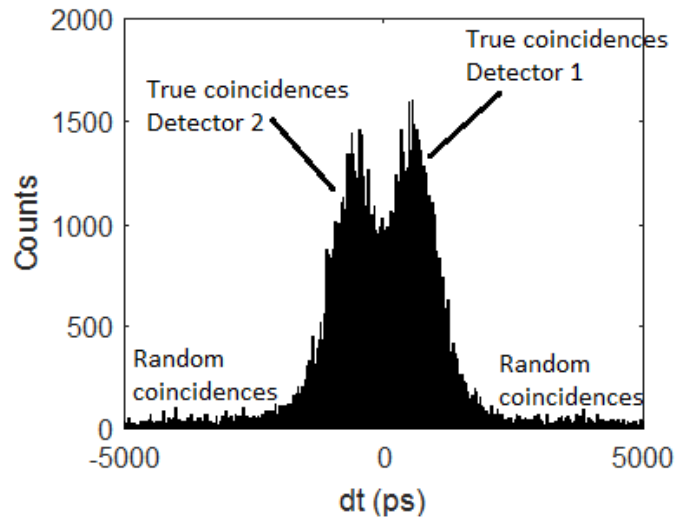


Figure 5.3: Time histogram of the zero measurement without the source and the distinction between true intrinsic coincidences happening in detector 1 and in detector 2 and the random intrinsic coincidences.

Bibliography

- [1] Beverly Riley, Peaking Into the Future With Proton Therapy, *Journal of Radiology Nursing* 26 (2007) 115-120.
- [2] WP Levin, H Kooy, JS Loeffler and TF DeLaney, Minireview Proton beam therapy, *British Journal of Cancer* 93 (2005) 849–854.
- [3] Matthew T Studenski, Ying Xiao, Proton therapy dosimetry using positron emission tomography, *World Journal of Radiology* 28 (2010) 135-142.
- [4] Thomas Frach et al., The digital Silicon Photomultiplier - A novel sensor for the detection of scintillation light, *Nuclear Science Symposium Conference Record* (2009) J04-1.
- [5] Wayne D Newhauser, Rui Zhang, The physics of proton therapy, *Physics in medicine and biology* 60 (2015) R155–R209.
- [6] J. E. Turner, *Atoms, Radiation, and Radiation Protection*, Wiley-VCH, New York, 3 edition (2007).
- [7] H. Bethe, J. Ashkin, *Experimental Nuclear Physics*, ed. E. Segré, J. Wiley, New York, (1953) p. 253.
- [8] Simon R. Cherry, James A. Sorenson, Michael E. Phelps, *Physics in nuclear medicine*, fourth edition (2012) 74-82.
- [9] S. M. Sze, *Physics of semiconductor devices*, Wiley-Interscience 1969.
- [10] Marco Durante, Harald Paganetti. Nuclear physics in particle therapy: a review. *Reports on Progress in Physics* 79 (2016)
- [11] Xuping Zhu, Georges El Fakhri, Proton Therapy Verification with PET imaging, *Theranostics* 3 (2013) 731-740.
- [12] Institute of Medicine and National Research Council, *Advancing Nuclear Medicine Through Innovation*, The National Academies Press (2007) 36-37.
- [13] Simon R. Cherry, James A. Sorenson, Michael E. Phelps, *Physics in nuclear medicine*, fourth edition (2012) 307-308.

- [14] York Haemisch, Thomas Frach, Carsten Degenhardt, Andreas Thon, Fully Digital Arrays of Silicon Photomultipliers (dSiPM) - a Scalable Alternative to Vacuum Photomultiplier Tubes (PMT), *Physics Procedia* 37 (2012) 1546-1560.
- [15] Philips Digital Photon Counting Module-TEK User Manual, 2014
- [16] P Campraia Lopes et al., First in situ TOF-PET study using digital photon counters for proton range verification, *Physics in Medicine and Biology* 61 (2016) 6203-6230.
- [17] Qingyang Wei, Tianyu Ma, Shi Wang, Yaqiang Liu, Yu Gu, Tiantian Dai, PET/CT alignment calibration with a non-radioactive phantom and the intrinsic ^{176}Lu radiation of PET detector, *Nuclear Instruments and Methods in Physics Research A* 835 (2016) 163–168.
- [18] Rihua Mao, Liyuan Zhang, Ren-Yuan Zhu, Optical and Scintillation Properties of Inorganic Scintillators in High Energy Physics, *IEEE Transactions on Nuclear Science* 55 (2008) 2425-2431.
- [19] Z.Liu et al. In-depth study of single photon time resolution fo the Philips digital silicon photomultiplier, *Journal of Instrumentation* 11 (2016) 6006
- [20] Matthew W. Fishburn. *Fundamentals of CMOS Single-Photon Avalanche Diodes*, 2012.
- [21] Sun Il Kwon, Jae Sung Lee, Signal encoding method for a time-of-flight PET detector using silicon photomultiplier array, *Nuclear Instruments and Methods in Physics Research A* 761 (2014) 39-45

Appendix A

PDPC instructions

The detector modules are controlled by DPCShell, which is a console based Linux program for the configuration and operation of the setup. This appendix explains step by step how the detector modules were operated by this program during the experiments by showing the used commands in chronological order written in **command font** followed by a brief description of the command.

To start the program open a terminal window and enter the command:

dpcshell

Now the DPCShell is opened. To properly start the setup the following commands should be entered

power up

Sets operating voltages and initializes the system

power show

Shows current voltages and currents

test jtag

Checks the configuration chain of the tile sensors

test tdc

Test the sensor dies TDC's by triggering the sensors via external delay loops

Now that the detectors are powered, they have to be set to the right temperature via the Peltier elements. This is done by setting the Peltier elements to about 3 volts on the control base unit. Then the desired acquisition parameters should be set with the configuration commands:

config set --validation 32 --trigger 4

Sets the validation scheme to 32 and the trigger scheme to 4

config show

Shows the currently configured settings to check if they are correct

config capture -c 4

config set --rtl-refresh off

Disables the rtl-refresh possibility

The right voltage settings have to be set for a stable tile temperature:

capture activate

tile info

Prints the information about all tiles. Check multiple times if the temperature is more or less stable

vbias adjust

Adjust the currently set bias voltage to the current tile temperature

capture deactivate

Now the modules have to be calibrated for dark counts:

vbias scan

Increases the tile sensor bias voltage, until a cell breakdown is detected, which gives the breakdown voltage for this tile sensor at the current temperature.

measure dcm --frames 1000

Measures an extended dark-count map (dcm) for 1000 frames

calibrate inhibit --generate=20 --upload

Generates and uploads an inhibit dark-count map and disables 20% of the cells with the highest dark count rate

calibrate tdc --generate --upload

Now the system is calibrated and all the operating parameters are set, it is time to

start the measurement:

```
capture --nframes 1000000
```

Capturing single events for one million frames. This number can be varied.

Appendix B

Time Skew Correction

In this appendix the time skew correction principle will be explained in detail, but first we have a look at the notation of the variables.

- P_{ijk} : Timestamp value of a single event generated by die i on tile j of detector k.
- ToF_{ijk} : Time of flight of a photon detected by die i on tile j of detector k.
- S_{ijk} : Skew of die i on tile j of detector k.

$$P_i = ToF_i + S_i$$

- $\Delta T_{ijk,uvw}$: Difference in timestamp generated by die i on tile j of detector k and die u on tile v of detector w.

$$\begin{aligned}\Delta T_{ijk,uvw} &= P_{uvw} - P_{ijk} \\ &= (ToF_{uvw} + S_{uvw}) - (ToF_{ijk} + S_{ijk}) \\ &= ToF_{uvw} - ToF_{ijk} + S_{uvw} - S_{ijk}\end{aligned}\tag{B.1}$$

- $\Delta ToF_{ijk,uvw}$: Real time of flight difference between two annihilation photons of a coincidence event detected by die i and die j, where the difference between i and j should be at least 64.

$$\Delta ToF_{ijk,uvw} = ToF_{uvw} - ToF_{ijk}$$

- $\Delta S_{ijk,uvw}$: Difference in time skew between die i on tile j of detector k and die u on tile v of detector w.

$$\Delta S_{ijk,uvw} = S_{uvw} - S_{ijk}\tag{B.2}$$

so,

$$\Delta T_{ijk,uvw} = \Delta T_{oF_{ijk,uvw}} + \Delta S_{ijk,uvw}$$

and so for a coincidence event the recorded timestamp difference $\Delta T_{ijk,uvw}$ between die i on tile j of detector k and die u on tile v of detector w can be corrected to get the actual real time of flight difference of the two annihilation photons by

$$\Delta T_{oF_{ijk,uvw}} = \Delta T_{ijk,uvw} - \Delta S_{ijk,uvw} \quad (\text{B.3})$$

So now we know how to correct for the time skew of the detectors if a coincidence event is detected between two dies on the opposing detectors. To obtain these values, we first take the difference in timestamp values between the central reference dies that corresponds to each other obtained in the two measurements with the source directly on the detectors. That means $\Delta T_{1611,322}$, $\Delta T_{321,1612}$, $\Delta T_{331,1642}$, and $\Delta T_{1641,332}$. For all four combinations, there are two values, one for each measurement, and let's call them $\Delta T1_{ijk,uvw}$ and $\Delta T2_{ijk,uvw}$. We have then

$$\begin{aligned} \Delta T1_{ijk,uvw} &= \Delta T_{oF1_{ijk,uvw}} + \Delta S1_{ijk,uvw} \\ \Delta T2_{ijk,uvw} &= \Delta T_{oF2_{ijk,uvw}} + \Delta S2_{ijk,uvw} \end{aligned}$$

and,

$$\Delta T1_{ijk,uvw} + \Delta T2_{ijk,uvw} = \Delta T_{oF1_{ijk,uvw}} + \Delta S1_{ijk,uvw} + \Delta T_{oF2_{ijk,uvw}} + \Delta S2_{ijk,uvw}. \quad (\text{B.4})$$

Since the position of the source is swapped in the two measurements, and the distance between the detectors stays the same, we know that

$$\begin{aligned} \Delta T_{oF1_{ijk,uvw}} &= -\Delta T_{oF1_{ijk,uvw}} \\ \Delta S1_{ijk,uvw} &= \Delta S2_{ijk,uvw} \end{aligned} \quad (\text{B.5})$$

So B.4 becomes

$$\Delta T1_{ijk,uvw} + \Delta T2_{ijk,uvw} = 2\Delta S_{ijk,uvw}. \quad (\text{B.6})$$

Now we have eliminated the time of flight part of the timestamp values and we are left with the skews of the four reference die combinations. Since we also know the skews between all four reference dies (or the skews between the tiles) and all the skews between the constituting dies on each tile, we eventually can calculate the skews, $\Delta T_{oF_{ijk,uvw}}$, of all combinations of dies that detect annihilation photons from a coincidence event.

For example, if we want to know the skew that has to be correct when die 13 of tile 3 on detector 1 and die 2 of tile 1 on detector 2 detect a coincidence event, we can not directly use equation B.4 ¹. Instead we write,

$$\begin{aligned}
\Delta S_{1331,212} &= S_{212} - S_{1331} \\
&= S_{212} - S_{1331} + S_{1612} - S_{1612} + S_{1642} - S_{1642} + S_{331} - S_{331} \\
&= (S_{212} - S_{1612}) + (S_{1612} - S_{1642}) + (S_{1642} - S_{331}) + (S_{331} - S_{1331}) \\
&= \Delta S_{1612,212} + \Delta S_{1642,1612} + \Delta S_{331,1642} + \Delta S_{1331,331},
\end{aligned}$$

which are all known.

¹Except if we perform the two measurements with the source swapped for each die combination, but therefore you will need 128 measurements.